Three-Dimensional Modeling of Glacier Flow and Bed Evolution in Subtropical Taiwan

Hsueh-Chen Lee

Wenzao Ursuline University of Languages, Taiwan

Preprint Status

This manuscript is a non-peer-reviewed preprint submitted to EarthArXiv.

ORCID: https://orcid.org/0000-0003-1783-9606

Corresponding author: 87013@mail.wzu.edu.tw

Three-Dimensional Numerical Modeling of Glacier Flow and U-Shaped Valley Evolution in Subtropical Taiwan

Hsueh-Chen Lee[a]

[a] *Center for General Education, Wenzao Ursuline University of Languages, Kaohsiung, Taiwan*

Abstract

Glacial erosion plays a critical role in shaping alpine topography, yet the coupled effects of ice deformation, basal sliding, and bedrock erosion on millennial-scale valley morphodynamics remain challenging to quantify. This study presents three-dimensional simulations of glacier dynamics and bed evolution in Xue Mountain Glacial Cirque No. 2, Taiwan, over an effective glaciation timescale of 9 ka. The nonlinear Stokes equations with Glen's flow law are solved using a stabilized equal-order Galerkin least-squares finite element method coupled with a basal sliding law, an empirical erosion law, and an Arbitrary Lagrangian–Eulerian moving-mesh formulation. Numerical experiments evaluate how ice thickness and the basal sliding constant govern long-term bed lowering and valley development. Spatially concentrated basal erosion along the valley axis progressively deepens and widens an initially V-shaped valley, producing a characteristic U-shaped cross-section. Sensitivity analyses reveal nonlinear coupled effects of ice thickness and the basal sliding constant on bed-normal lowering distance, as increasing ice thickness enhances basal sliding velocity and, consequently, subglacial erosion rates. Using the present-day valley-floor elevation as a geomorphic constraint yields a physically plausible reconstruction of former glacier conditions. After 9 ka, the reconstructed bed profile reproduces the smooth U-shaped morphology, with a minimum elevation of 3716.6 m, only 0.6 m above the present-day valley-floor elevation of 3716 m used as a constraint. These findings demonstrate how integrated flow–sliding–erosion modeling provides quantitative insights into the long-term morphodynamic evolution of subtropical alpine glacial landscapes.

Keywords: glacier flow; glacier-bed evolution; glacial cirque; basal sliding; bedrock erosion; finite element method; subtropical glaciation

Email address: 87013@mail.wzu.edu.tw (Hsueh-Chen Lee)

1. Introduction

> "The towering mountains, the verdant forests, the rich diversity of flora and fauna, and the mountain life of the Indigenous peoples were interwoven into a world of mountains that completely captivated me."
>
> — Tadao Kano, 1941 (Kano, 2000, p. 32)
> *(English translation by the author)*

In 1926, Japanese naturalist and geographer Tadao Kano began exploring the Xue Mountain region in Taiwan. His field investigations identified 35 glacial cirques and other glacial landforms, providing some of the earliest evidence of past glaciation in Taiwan (National Parks of Taiwan, 2026; Cui et al., 2002). Nearly a century later, these landforms remain important geomorphic records of past glacier activity in Taiwan's high mountains.

Taiwan lies in a subtropical region and has no glaciers today. Nevertheless, the Xue Mountain range rises above 3500 m and preserves remarkable landforms associated with former glaciation. Xue Mountain Glacial Cirque No. 1 is the largest, whereas Cirque No. 2 is among the best-preserved glacial cirques in Taiwan (Cui et al., 2002; Lee, 2026). The location and present-day morphology of Cirque No. 2 are shown in Figure 1. These glacial landforms constitute a persistent topographic legacy of former glacier activity in Taiwan's high mountains. In a broader sense, the close association between mountain landscapes and biological diversity noted by Kano is also reflected in modern phylogeographic studies of Taiwan's alpine environments (Weng et al., 2016). The well-preserved geometry of Cirque No. 2 therefore provides a valuable natural setting for investigating how long-term glacier flow, basal sliding, and bedrock erosion contributed to the development of the present-day glacial landscape.

Glacial valleys are commonly characterized by U-shaped transverse profiles produced by the combined effects of glacier flow, basal sliding, and bedrock erosion over long timescales. Because these processes operate over timescales of thousands of years, their cumulative effects cannot be directly observed. Numerical modeling therefore provides a valuable means of investigating glacier dynamics, basal erosion, and landscape evolution over millennial timescales (Harbor, 1992; MacGregor et al., 2000; Yang and Shi, 2015). Seddik et al. (2009) further suggested that extending valley-evolution models to three dimensions could provide a more complete description of both transverse and longitudinal evolution. This perspective offers strong motivation for developing three-dimensional models that couple glacier dynamics with long-term bed evolution.

Numerical models of glacial landscape evolution have progressively incorporated more complete representations of glacier dynamics and erosional processes. Jamieson et al.

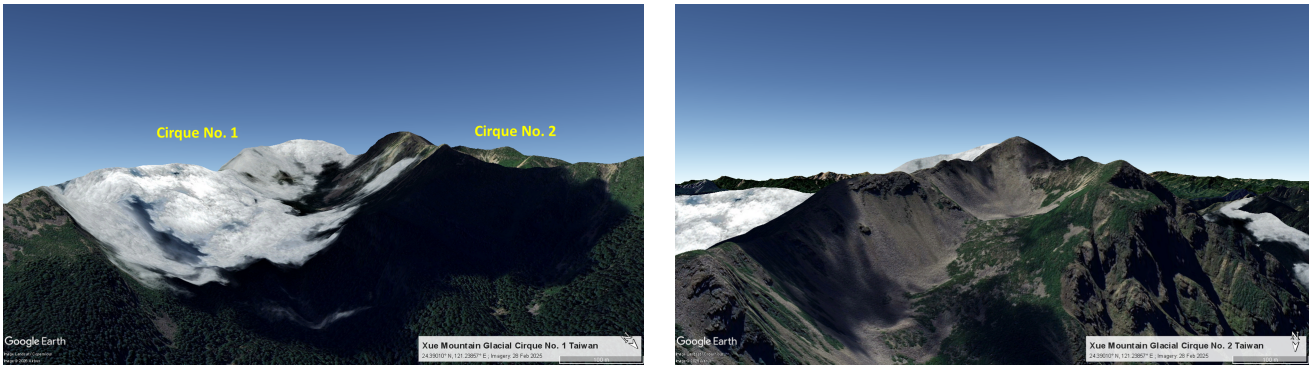

(a) Cirques Nos. 1 and 2 (b) Cirque No. 2

Figure 1: Google Earth views of the Xue Mountain Glacial Cirques, Taiwan: (a) overview of Glacial Cirques Nos. 1 and 2; (b) close-up view of Glacial Cirque No. 2, the study area.

(2008) coupled a three-dimensional thermomechanical ice-sheet model with basal sliding and erosion to investigate long-term landscape evolution. Egholm et al. (2012b) subsequently demonstrated through three-dimensional computational experiments that higher-order ice dynamics and horizontal stress gradients can substantially influence basal shear stress and the feedback between glacier sliding and erosion. Egholm et al. (2012a) further developed a three-dimensional landscape evolution framework coupling the flow of ice, water, and sediment, allowing simulated glacial landforms to be compared directly with existing topography. These studies highlight the importance of three-dimensional glacier dynamics for understanding long-term landscape evolution, particularly in steep alpine terrain.

Many long-term glacial landscape evolution models employ shallow-ice or higher-order approximations to reduce computational cost, as repeatedly solving the full nonlinear Stokes equations—especially in three dimensions with an evolving bed geometry—remains computationally demanding. The Galerkin least-squares (GLS) formulation offers a robust and practical solution to this numerical challenge. By incorporating residual-based stabilization, the GLS approach enables equal-order velocity-pressure interpolations, thereby bypassing the classical inf-sup stability constraint inherent in standard Galerkin finite element (GFE) methods (Lee and Lee, 2026a). This equal-order discretization substantially simplifies the finite-element implementation, facilitates mesh updating in evolving domains (e.g., Arbitrary Lagrangian-Eulerian (ALE) formulations), and reduces the total degrees of freedom compared to higher-order mixed formulations.

Previous studies established the numerical and theoretical foundations for this approach. Lee et al. (2024) demonstrated that a stabilized GLS formulation provides

accurate and stable solutions for steady tidewater-glacier flow. Subsequently, Lee and Lee (2026b) developed a stabilized equal-order (P_1, P_1) GLS formulation for the nonlinear Stokes equations and established its theoretical error estimates. Similar stabilized equal-order formulations have also proven effective in other nonlinear flow contexts, such as porous-media and generalized Newtonian pore-scale flows (Lee and Lee, 2024, 2026a). Furthermore, Lee (2026) established a two-dimensional framework for long-term glacier-bed evolution by coupling basal sliding with bedrock erosion.

Geomorphological and paleoclimatic evidence indicates widespread alpine glaciation during the Last Glacial Maximum (LGM), approximately 27–18 ka (Clark et al., 2009; Asami et al., 2021; Lee, 2026). Accordingly, an effective glaciation timescale of approximately 9 ka is adopted in the present study to evaluate the cumulative effects of glacier flow and basal erosion. Glacier ice is modeled as an incompressible, shear-thinning material governed by Glen's flow law (Glen, 1955; Greve and Blatter, 2009). By incorporating longitudinal bed slope and three-dimensional ice flow, the model explicitly resolves spatial variations in basal sliding and erosion, simulating the long-term evolution of an initially V-shaped valley over this interval.

Building on this foundation, the present study extends the stabilized equal-order GLS formulation to three-dimensional nonlinear Stokes glacier flow and couples it with basal sliding and bedrock erosion. The study addresses three primary objectives: (1) to develop a computationally practical three-dimensional GLS framework for nonlinear glacier flow and long-term bed evolution; (2) to quantify the individual and combined influences of ice thickness and basal sliding constant on bed erosion and valley lowering; and (3) to examine whether the modeled evolution of an initially V-shaped valley can reproduce the present-day U-shaped morphology of Xue Mountain Glacial Cirque No. 2 and thereby constrain plausible former glacier conditions.

The Xue Mountain case therefore serves both as a physically constrained reconstruction of a subtropical glacial landscape and as a benchmark for evaluating the applicability of the stabilized equal-order GLS framework to physically meaningful three-dimensional simulations of glacier dynamics and long-term morphodynamic evolution.

The remainder of this paper is organized as follows. Section 2 presents the mathematical model, including the three-dimensional geometry, glacier-bed evolution model, governing equations, boundary conditions, and GLS weak formulation. Section 3 describes the numerical method and solution strategy. Section 4 presents the numerical results. Section 5 discusses the main findings and their geomorphological and numerical implications. Finally, Section 6 summarizes the main conclusions.

2. Model Description

2.1. Problem statement and three-dimensional geometry

Figure 2(a) shows the topographic contour map of Xue Mountain Glacial Cirque No. 2 obtained from the Taiwan online topographic database (Happyman GIS Project, 2025). The topographic data are used to extract elevation information for constructing the numerical model. A three-dimensional stepped terrain model is subsequently generated from the topographic contours using the CAD software SpaceClaim (SpaceClaim Corporation, 2026), as illustrated in Figure 2(b).

The transverse section A–M–B is selected to characterize the cross-valley geometry, where A and B denote the left and right valley-side points, respectively, and M denotes the valley-floor point along the longitudinal centerline C–M–L. The points C and L represent the upstream and downstream limits of the centerline, which approximately aligns with the main downslope direction of the cirque. The coordinates and elevations of these reference points (A, B, M, C, and L) are summarized in Table 1.

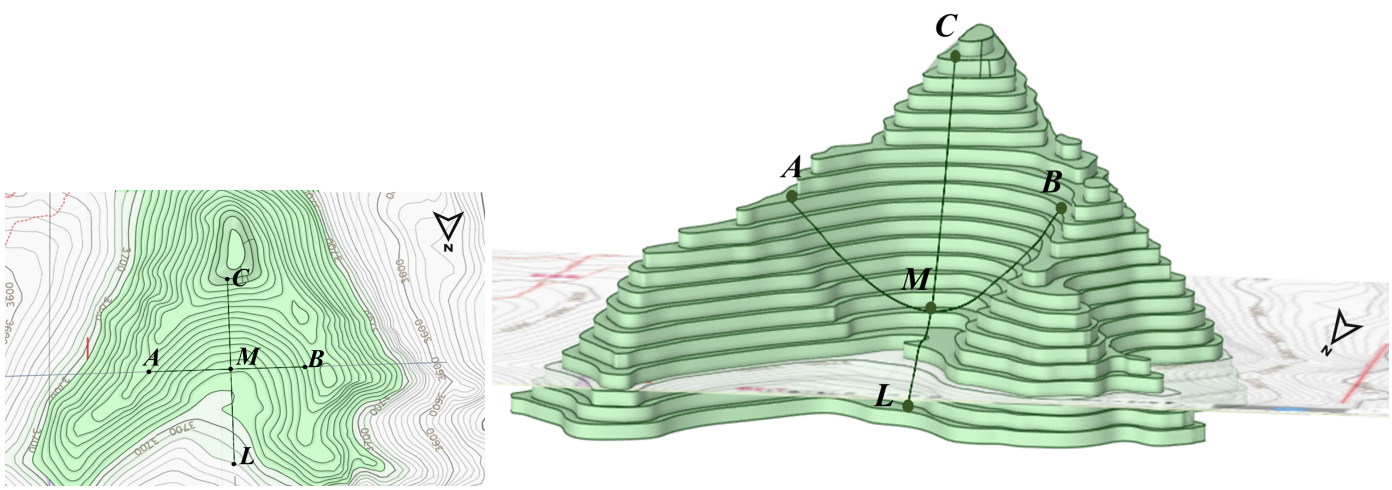

(a) Topographic Map

(b) Three-dimensional terrain model

Figure 2: Topographic map and three-dimensional terrain model of Xue Mountain Glacial Cirque No. 2. (a) Topographic map (Happyman GIS Project, 2025) showing the transverse section A–M–B and longitudinal centerline C–M–L; (b) three-dimensional terrain model constructed using ANSYS SpaceClaim (SpaceClaim Corporation, 2026).

Table 1: Physical, geometric, and model parameters used in this study.

Parameter	Symbol	Value	Units
Ice density	ρ	918	$\mathrm{kg\,m^{-3}}$
Gravity	g	9.81	$\mathrm{m\,s^{-2}}$
Glen's flow-law exponent	n	3	–
Pre-exponential constant	A_0	1.916×10^3	$\mathrm{s^{-1}\,Pa^{-3}}$
Activation energy	Q	139	$\mathrm{kJ\,mol^{-1}}$
Universal gas constant	R	8.314	$\mathrm{J\,K^{-1}\,mol^{-1}}$
Absolute ice temperature	T'	264.15 (-9°C)	K
Initial slope-normal ice thickness range	H	30–60	m
Valley half-width	W	105	m
Bed-normal lowering distance	d_b	–	m
Left valley-side point	A	$(-105,\ 3790,\ 0)$	m
Right valley-side point	B	$(98,\ 3790,\ 0)$	m
Present-day valley-floor point	M	$(0,\ 3716,\ 0)$	m
Upstream centerline point	C	$(0,\ 3860,\ -84)$	m
Downstream centerline point	L	$(0,\ 3680,\ 175)$	m
Idealized mirror point of A about $x = 0$	A'	$(105,\ 3790,\ 0)$	m
Mean longitudinal slope angle	β	34.8	°
Longitudinal distance between C and L	L_{CL}	316	m
Basal sliding constant	C_b	30–50	$\mathrm{m\,a^{-1}\,MPa^{-1}}$
Erosion constant	C_e	10^{-4}	$\mathrm{a\,m^{-1}}$

Using the transverse profile A–M–B (Fig. 2), Figure 3 compares the present-day valley cross-profile with the idealized V-shaped profile adopted as the initial glacier bed. The present-day valley cross-section exhibits approximate symmetry about the centerline, with the valley-side points A and B positioned approximately symmetrically relative to M. The initial glacier-surface elevation at point A is $y_A = 3790$ m, whereas the present-day bed elevation at point M is $y_M = 3716$ m. Here, H_y denotes the vertical ice thickness and $d_{b,y}$ the vertical bed-lowering distance. The corresponding geometric constraint is therefore $H_y + d_{b,y} = y_A - y_M = 74$ m.

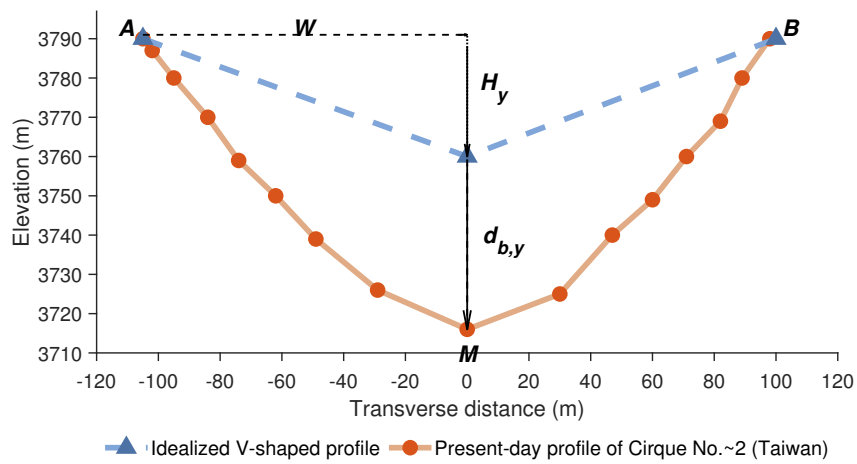

Figure 3: Comparison of the present-day valley cross-profile of Xue Mountain Cirque No. 2 (Taiwan) with the initial V-shaped profile, illustrating the valley half-width W, vertical ice thickness H_y, and vertical bed-lowering distance $d_{b,y}$.

Figure 4 schematically illustrates the three-dimensional glacier geometry used to model the evolution of an initially V-shaped valley into a U-shaped glacial valley over the 9 ka simulation period. Here, H denotes the ice thickness, d_b the bed-normal lowering distance, W the valley half-width, and β the longitudinal slope angle. The colored contours represent the pressure distribution, which is further examined in the numerical results presented in Section 4. A Cartesian coordinate system (x, y, z) is adopted, where x, y, and z denote the transverse, vertical (elevation), and longitudinal horizontal directions, respectively. Owing to the approximately symmetric valley geometry, the half-section A–M, extending from the left valley side to the valley center, is used to construct the three-dimensional half-domain. The point A' denotes the idealized mirror

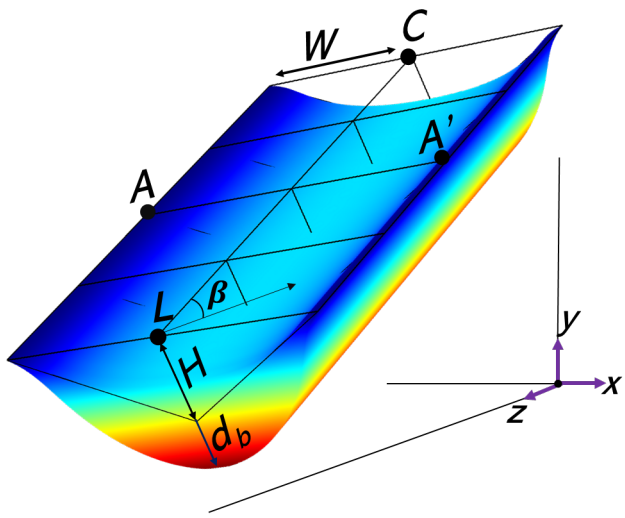

Figure 4: Schematic illustration of the three-dimensional glacier geometry and pressure contours.

point of A about the symmetry plane $x = 0$. This symmetry reduces the computational domain and simplifies the subsequent numerical simulations.

The mean longitudinal bed-slope angle β is determined from the elevation difference and longitudinal horizontal separation between points C and L in Figure 4. Based on the coordinates given in Table 1, these distances are 180 m and 259 m, respectively. Thus,

$$\beta = \tan^{-1}\left(\frac{180}{259}\right) \approx 34.8^\circ. \tag{2.1}$$

As illustrated in Figure 4, H denotes the bed-normal ice thickness, and d_b represents the bed-normal lowering distance. Their corresponding vertical components are defined as $H_y = H\cos\beta$ and $d_{b,y} = d_b\cos\beta$, where β is the bed slope angle. Applying the geometric constraint $H_y + d_{b,y} = 74$ m derived from the present-day valley cross-profile (Fig. 3) yields

$$H + d_b = \frac{74}{\cos\beta} \approx 90.1 \text{ m}. \tag{2.2}$$

2.2. Glacier-bed evolution model

To investigate whether an initially V-shaped valley in Xue Mountain Glacial Cirque No. 2 could gradually evolve toward a U-shaped glacial valley, glacier flow is coupled with a basal erosion model over a long-term evolution period.

Glacial erosion results from several processes, including abrasion, plucking, subglacial fluvial erosion, and chemical dissolution (Harbor, 1992; Lee, 2026). Because of the complexity of subglacial processes and bed conditions, a fully mechanistic description of bedrock erosion remains difficult. Empirical erosion laws are therefore commonly used to represent the net erosion rate normal to the bedrock surface. In the present model, the erosion rate is related to the basal sliding velocity by

$$E = C_e u_b^2, \tag{2.3}$$

where E is the erosion rate, u_b is the basal sliding velocity, and C_e is the erosion constant, (Hallet, 1979; Harbor, 1992; MacGregor et al., 2000; Seddik et al., 2009). Values of C_e adopted in previous glacier-erosion studies are typically in the range 10^{-5}–10^{-4} $\mathrm{a\,m^{-1}}$ (MacGregor et al., 2000; Yang and Shi, 2015; Lee, 2026).

In our previous two-dimensional study of Xue Mountain Glacial Cirque No. 2 (Lee, 2026), the effects of ice thickness, basal sliding, and the erosion constant on the predicted erosion timescale were systematically examined. Using values at $Ce = 8 \times 10^{-5}$, 10^{-4}, 1.2×10^{-4}, and $Ce = 2 \times 10^{-4}$ $\mathrm{a\,m^{-1}}$ in the studies, the results illustrate how the fitted relationship varies across the empirical range of the erosion constant and provide a sensitivity view of the admissible parameter region. For the reference value $C_e = 10^{-4}$ $\mathrm{a\,m^{-1}}$, the admissible combinations of ice thickness and basal sliding constant were constrained using an effective LGM glaciation duration of 9 ka. The sensitivity analysis further showed that the combinations of ice thickness and basal sliding constant required to reproduce the 9 ka timescale depend on C_e, demonstrating the coupled influence of glacier geometry, basal sliding, and erosion efficiency on long-term bed evolution. Accordingly, $C_e = 10^{-4}$ $\mathrm{a\,m^{-1}}$ is adopted as the reference erosion constant in the present three-dimensional simulations.

The flowchart of the glacier-bed evolution model is shown in Figure 5. Figure 5 summarizes the coupling between glacier flow, basal sliding, and bed erosion. Starting from the initial V-shaped valley geometry, the nonlinear Stokes equations are solved to obtain the glacier-flow field and the basal sliding velocity u_b. The bed geometry is then updated according to the erosion law in (2.3). This coupled procedure is repeated at each time step until $t = 9$ ka.

2.3. Governing equations

Let $\Omega \subset \mathbb{R}^d$, $d = 2, 3$ be a bounded Lipschitz domain with boundary Γ. The stationary incompressible nonlinear Stokes equations governing glacier flow are given by (Chen et al., 2013)

$$-\nabla \cdot \boldsymbol{\sigma} = \mathbf{f} \quad \text{in } \Omega, \tag{2.4}$$

$$\nabla \cdot \mathbf{u} = 0 \quad \text{in } \Omega, \tag{2.5}$$

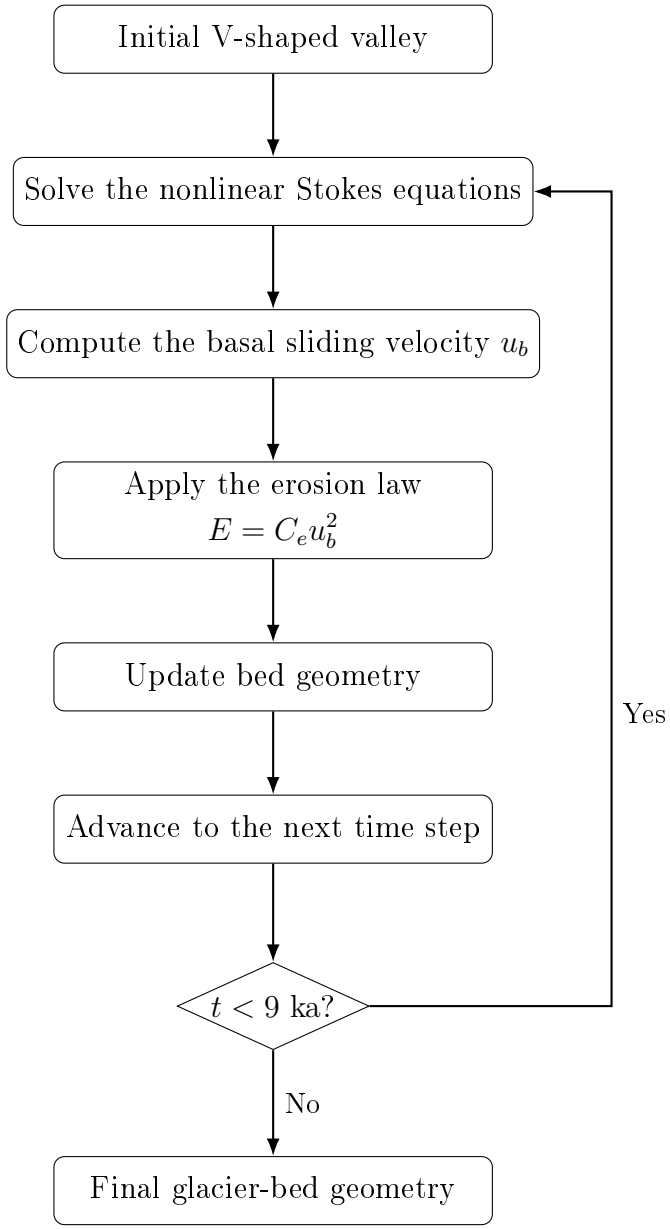

Figure 5: Flowchart of the glacier-bed evolution model.

where $\mathbf{u}$ is the velocity field and $\mathbf{f} = \rho\mathbf{g}$ is the gravitational body force with the ice density ρ and, since the y-axis is taken as the vertical direction, $\mathbf{g} = (0, -g, 0)^\top$, with the gravitational acceleration g.

The Cauchy stress tensor is defined as $\boldsymbol{\sigma} = \boldsymbol{\tau} - p\mathbf{I}$ with pressure p. The extra stress tensor $\boldsymbol{\tau}$ is defined as $\boldsymbol{\tau} = 2\eta(\mathbf{u})\mathbf{D}(\mathbf{u})$ with the strain-rate tensor $\mathbf{D}(\mathbf{u}) = \frac{1}{2}\left(\nabla\mathbf{u} + \nabla\mathbf{u}^\top\right)$.

The rheological behavior of glacier ice is described by Glen's flow law (Glen, 1955), in which the shear-thinning behavior is represented through the effective viscosity

$$\eta(\mathbf{u}) = \mu\,\dot{\gamma}(\mathbf{u})^{\frac{1-n}{n}}, \tag{2.6}$$

$$\dot{\gamma}(\mathbf{u}) = \sqrt{\frac{1}{2}\,\mathrm{tr}\big[\mathbf{D}(\mathbf{u})^2\big]}, \tag{2.7}$$

where n is Glen's flow-law exponent, typically taken as $n = 3$ in glaciological applications (Greve and Blatter, 2009), and $\mu = \frac{1}{2}A(T')^{-1/n}$. The temperature-dependent flow-rate factor $A(T')$ is described by an Arrhenius-type relation (Greve and Blatter, 2009), $A(T') = A_0 \exp\left(-\frac{Q}{RT'}\right)$, where T' denotes the absolute ice temperature, A_0 is the pre-exponential constant, Q is the activation energy, and R is the universal gas constant. In the present simulations, an ice temperature of $-9°$C, corresponding to $T' = 264.15$ K, is adopted in (Lee and Lee, 2026b). The material parameters are taken from standard glacier-flow models and our previous studies (Lee et al., 2024; Lee and Lee, 2026b; Lee, 2026). The symbols and parameter values used in the present study are summarized in Table 1.

To treat the nonlinearity arising from the strain-rate-dependent viscosity, Picard iteration is employed. Let $\mathbf{u}_k$ denote the known velocity approximation at iteration k, with the initial guess $\mathbf{u}_0 = \mathbf{0}$. Since the effective strain rate $\dot{\gamma}(\mathbf{u}_k)$ may approach zero, the viscosity in (2.6) may become singular. We therefore introduce the regularized effective strain rate $\dot{\gamma}_{\mathrm{reg}}(\mathbf{u}_k) = \max\left\{\dot{\gamma}(\mathbf{u}_k), \dot{\gamma}_{\min}\right\}$, with a prescribed regularization parameter $\dot{\gamma}_{\min} > 0$. A sensitivity analysis of the regularization parameter was performed in our previous studies (Lee and Lee, 2026a,b), where values ranging from 10^{-10} to 10^{-18} s^{-1} were examined and found to have negligible effects on the numerical results and convergence behavior. Accordingly, $\dot{\gamma}_{\min} = 10^{-15}$ s^{-1} is adopted in the present simulations.

At iteration k, the viscosity is evaluated using the current velocity iterate $\mathbf{u}_k$ as $\eta_k = \mu\,\dot{\gamma}_{\mathrm{reg}}(\mathbf{u}_k)^{\frac{1-n}{n}}$. The Picard linearization then yields the following variable-viscosity Stokes problem: given $\mathbf{u}_k$, find $(\mathbf{u}_{k+1}, p_{k+1})$ such that

$$-\nabla\cdot\big(2\eta_k\mathbf{D}(\mathbf{u}_{k+1})\big) + \nabla p_{k+1} = \mathbf{f} \quad \text{in } \Omega, \tag{2.8}$$

$$\nabla\cdot\mathbf{u}_{k+1} = 0 \quad \text{in } \Omega. \tag{2.9}$$

2.4. Boundary conditions

The glaciological Stokes system (2.4)–(2.5) is closed by prescribing physically relevant boundary conditions (Monnesland et al., 2016; Lee et al., 2024). The boundary of the computational domain is decomposed as

$$\Gamma = \Gamma_s \cup \Gamma_{\text{sym}} \cup \Gamma_b \cup \Gamma_{\text{in}} \cup \Gamma_{\text{out}},$$

where Γ_s denotes the upper slip surface, Γ_{sym} the symmetry boundary, Γ_b the ice–bedrock interface, and Γ_{in} and Γ_{out} the inflow and outflow boundaries, respectively. The computational domain, boundary decomposition, and computational mesh are illustrated in Figure 6.

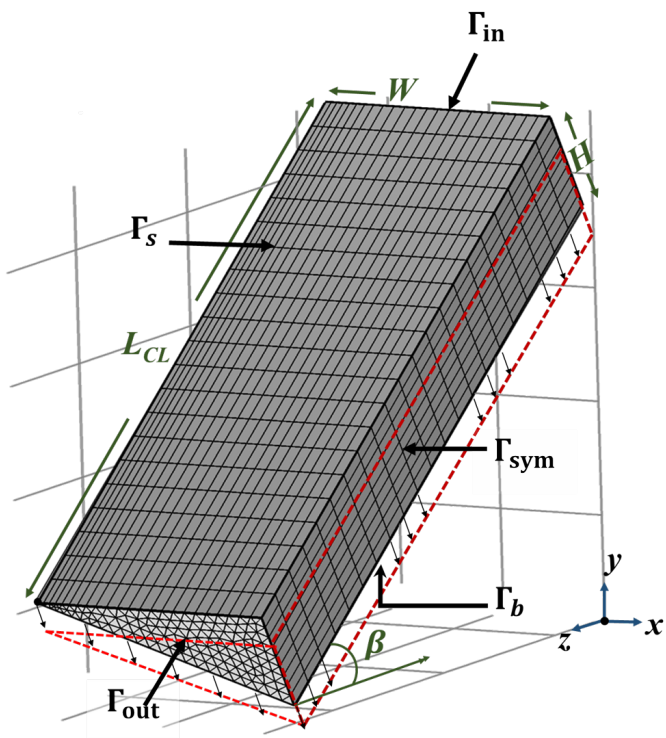

Figure 6: Computational domain, boundary decomposition, and computational mesh of the three-dimensional glacier model.

For the three-dimensional formulation, the tangential projection operator is defined by

$$\mathbf{P}_t = \mathbf{I} - \mathbf{n} \otimes \mathbf{n},$$

where $\mathbf{n}$ denotes the outward unit normal vector. The tangential velocity is defined as

$$\mathbf{u}_t = \mathbf{P}_t \mathbf{u} = \mathbf{u} - (\mathbf{u} \cdot \mathbf{n})\mathbf{n}.$$

(i) Upper slip boundary.

On the upper surface Γ_s, an impermeable slip condition is imposed:

$$\mathbf{u} \cdot \mathbf{n} = 0, \qquad \mathbf{P}_t(\boldsymbol{\sigma}\mathbf{n}) = \mathbf{0} \quad \text{on } \Gamma_s. \tag{2.10}$$

The first condition prevents flow across the upper surface, while the second imposes zero tangential traction, allowing the ice to move freely along the surface.

(ii) Symmetry boundary.

Because only one half of the valley is included in the computational domain, a symmetry condition is imposed on Γ_{sym}, which corresponds to the valley-center plane $x = 0$. The normal velocity vanishes and the tangential traction is zero:

$$\mathbf{u} \cdot \mathbf{n} = 0, \qquad \mathbf{P}_t(\boldsymbol{\sigma}\mathbf{n}) = \mathbf{0} \quad \text{on } \Gamma_{\text{sym}}. \tag{2.11}$$

(iii) Basal sliding boundary.

On the ice–bedrock interface Γ_b, an impermeability condition together with a linear Navier sliding law is imposed:

$$\mathbf{u} \cdot \mathbf{n} = 0, \qquad \mathbf{P}_t(\boldsymbol{\sigma}\mathbf{n}) = -\frac{1}{C_b}\mathbf{u}_t \quad \text{on } \Gamma_b, \tag{2.12}$$

where $C_b > 0$ is the basal sliding constant controlling the magnitude of basal sliding (Navier, 1823; Monnesland et al., 2016; Greve, 2025).

In terms of the magnitudes of the tangential basal velocity and basal shear stress, the sliding law can be written as

$$u_b = C_b \, \tau_b, \tag{2.13}$$

with $u_b = \|\mathbf{u}_t\|$ and $\tau_b = \left\|\mathbf{P}_t(\boldsymbol{\sigma}\mathbf{n})\right\|$.

Equation (2.13) represents a linear Navier-type basal sliding law and can be regarded as a special case of the Weertman–Budd sliding law (Greve, 2025). In the frozen-bed limit, $C_b \to 0$, the tangential basal velocity vanishes, corresponding to $\mathbf{u}_t = \mathbf{0}$.

(iv) Inflow and outflow boundaries.

A lithostatic normal stress distribution is prescribed on the inflow Γ_{in} and outflow Γ_{out} boundaries, while the tangential velocity is constrained to zero. The prescribed pressure distributions are given by

$$p_{\text{in}}(y) = \rho g\,(y_{\text{max,in}} - y), \tag{2.14}$$

and

$$p_{\text{out}}(y) = \rho g\,(y_{\text{max,out}} - y), \tag{2.15}$$

where $y_{\text{max,in}}$ and $y_{\text{max,out}}$ denote the maximum elevations of the inflow and outflow boundaries, respectively.

The corresponding boundary conditions are

$$\mathbf{n}\cdot\boldsymbol{\sigma}\mathbf{n} = -p_{\text{in}}(y), \qquad \mathbf{u}_t = \mathbf{0} \quad \text{on } \Gamma_{\text{in}}, \tag{2.16}$$

and

$$\mathbf{n}\cdot\boldsymbol{\sigma}\mathbf{n} = -p_{\text{out}}(y), \qquad \mathbf{u}_t = \mathbf{0} \quad \text{on } \Gamma_{\text{out}}. \tag{2.17}$$

2.5. Galerkin weak formulation

Following (Lee et al., 2024), the velocity space is

$$H^1_\Gamma := \left\{ \mathbf{v} \in [H^1(\Omega)]^d \;\middle|\; \mathbf{v}\cdot\mathbf{n} = 0 \text{ on } \Gamma_s \cup \Gamma_{\text{sym}} \cup \Gamma_b,\ \mathbf{v}_t = \mathbf{0} \text{ on } \Gamma_{\text{in}} \cup \Gamma_{\text{out}} \right\}.$$

The pressure space is $Q := L^2(\Omega)$. Since the normal traction is prescribed on the inflow and outflow boundaries, the pressure level is determined by the boundary conditions given in (2.14)–(2.15), and no additional pressure normalization is required.

Let $\boldsymbol{\Phi} := H^1_\Gamma \times Q$. The Galerkin weak formulation of (2.8)–(2.9) with the boundary conditions (2.10)–(2.17) is to find $\boldsymbol{U} = (\mathbf{u}, p) \in \boldsymbol{\Phi}$ such that

$$\mathcal{B}(\boldsymbol{U}, \boldsymbol{V}) = \mathcal{F}(\boldsymbol{V}) \qquad \forall\, \boldsymbol{V} = (\mathbf{v}, q) \in \boldsymbol{\Phi}, \tag{2.18}$$

where

$$\mathcal{B}(\boldsymbol{U}, \boldsymbol{V}) = a(\mathbf{u}, \mathbf{v}) + b(\mathbf{v}, p) + b(\mathbf{u}, q) + c(\mathbf{u}, \mathbf{v}), \tag{2.19}$$

with

$$a(\mathbf{u},\mathbf{v}) = \int_\Omega 2\eta_k\, \mathbf{D}(\mathbf{u}) : \mathbf{D}(\mathbf{v})\, d\mathbf{x}, \tag{2.20}$$

$$b(\mathbf{v},p) = -\int_\Omega p\, \nabla\cdot\mathbf{v}\, d\mathbf{x}, \tag{2.21}$$

$$b(\mathbf{u},q) = \int_\Omega q\, \nabla\cdot\mathbf{u}\, d\mathbf{x}, \tag{2.22}$$

$$c(\mathbf{u},\mathbf{v}) = \int_{\Gamma_b} C_b^{-1}\, \mathbf{u}_t\cdot\mathbf{v}_t\, ds, \tag{2.23}$$

and

$$\begin{aligned}\mathcal{F}(\boldsymbol{V}) = &\int_\Omega \mathbf{f}\cdot\mathbf{v}\, d\mathbf{x} - \int_{\Gamma_{\text{in}}} p_{\text{in}}(y)\,(\mathbf{n}\cdot\mathbf{v})\, ds \\ &- \int_{\Gamma_{\text{out}}} p_{\text{out}}(y)\,(\mathbf{n}\cdot\mathbf{v})\, ds.\end{aligned} \tag{2.24}$$

3. Finite element approximation

For the finite element approximation, we assume that Ω is a polytopal domain and that $\mathcal{T}_h$ is a regular partition of Ω into finite elements such that $\Omega = \bigcup_{T\in\mathcal{T}_h} T$, with mesh size $h = \max_{T\in\mathcal{T}_h} \operatorname{diam}(T)$. The mesh $\mathcal{T}_h$ is assumed to satisfy the standard regularity and inverse estimates (Brenner and Scott, 2008). Let $P_m(T)$ denote the space of polynomials of degree at most m on an element T.

Define finite element spaces for the approximate of $\boldsymbol{U} = (\mathbf{u}, p)$:

$$\begin{aligned} H_\Gamma^{1,h} &= \left\{ \mathbf{v}^h \in H_\Gamma^1 \;\middle|\; \mathbf{v}^h|_T \in [P_m(T)]^3\ \forall T\in\mathcal{T}_h \right\}, \\ Q^h &= \left\{ q^h \in Q \;\middle|\; q^h\,|_T \in P_m(T)\ \forall T\in\mathcal{T}_h \right\}. \end{aligned}$$

Let $\boldsymbol{\Phi}^h := H_\Gamma^{1^h} \times Q^h$ be a finite element subspace of $\boldsymbol{\Phi}$ satisfies approximation property (Lee and Lee, 2026b). The GFE formulation for (2.18) is

$$\mathcal{B}(\boldsymbol{U}^h, \boldsymbol{V}^h) = \mathcal{F}(\boldsymbol{V}^h), \quad \forall \boldsymbol{V}^h \in \boldsymbol{\Phi}^h, \tag{3.1}$$

where the spaces $H_\Gamma^{1^h}$ and Q^h should be properly selected to satisfy the inf-sup condition for the stability of the finite element method.

The GLS formulation is obtained by introducing a stabilization parameter $\alpha > 0$ and the stabilization terms B_{DS} and F_{DS} into (3.1):

$$\mathcal{B}(\boldsymbol{U}^h, \boldsymbol{V}^h) + \alpha B_{DS}(\boldsymbol{U}^h, \boldsymbol{V}^h) = \mathcal{F}(\boldsymbol{V}^h) + \alpha F_{DS}(\boldsymbol{V}^h), \tag{3.2}$$

where

$$B_{DS}(\boldsymbol{U}^h, \boldsymbol{V}^h) = \sum_{T \in \mathcal{T}_h} h^2 \left(\frac{1}{\eta_k^h} \left[-\nabla \cdot \left(2\eta_k^h \mathbf{D}(\mathbf{u}^h) \right) + \nabla p^h \right], \nabla q^h \right), \tag{3.3}$$

$$F_{DS}(\boldsymbol{V}^h) = \sum_{T \in \mathcal{T}_h} h^2 \left(\frac{1}{\eta_k^h} \mathbf{f}, \nabla q^h \right), \tag{3.4}$$

with $\eta_k^h = \eta(\mathbf{u}_k^h)$. The stabilization parameter $\alpha > 0$ controls the strength of the GLS stabilization and may be selected according to the numerical characteristics of the problem (Donea and Huerta, 2003; Lee et al., 2024; Lee and Lee, 2024, 2026b).

For the standard Galerkin formulation, the discrete velocity and pressure spaces must satisfy the discrete inf-sup condition to ensure numerical stability. However, equal-order finite-element pairs often violate this classical stability constraint, leading to spurious pressure oscillations (Girault and Raviart, 1986). To overcome this limitation, equal-order polynomial interpolations are employed for the finite-element approximation of (2.18), integrated with GLS stabilization (Lee et al., 2024; Lee and Lee, 2024, 2026b). Recently, Lee and Lee (2026b) established the rigorous well-posedness and optimal finite-element error estimates of this stabilized equal-order formulation for the nonlinear Stokes problem.

Solution strategy

The three-dimensional glacier-flow model is coupled with basal sliding and bedrock erosion to simulate long-term valley morphodynamics. At each time step, the glacier domain geometry is fixed while the nonlinear Stokes system is solved iteratively using the stabilized equal-order GLS formulation in (3.2). The computed basal velocity field is subsequently used to evaluate the bedrock erosion rate. The resulting bed motion is accommodated using an Arbitrary Lagrangian-Eulerian (ALE) moving-mesh formulation, after which the glacier flow field is recalculated on the updated geometry. Because glacier dynamics adjust over much shorter time scales than long-term bedrock evolution, a successive quasi-steady state approximation is adopted. A numerical time step of $\Delta t = 100$ a is employed for the bed evolution, corresponding to 90 geometric updates across the 9 ka simulation period. The overall solution procedure is outlined in Algorithm 1.

The basal sliding velocity magnitude is defined as $u_b = \|\mathbf{u}_t\| = \sqrt{u^2 + v^2 + w^2} \quad \text{on } \Gamma_b$, where the second equality holds under the kinematic impermeability condition $\mathbf{u} \cdot \mathbf{n} = 0$ on Γ_b. In the ALE formulation, erosion-induced mesh displacement is constrained to the transverse-vertical (x, y) plane. Accordingly, the projection of the erosion-induced normal velocity onto this cross-sectional plane is prescribed on the glacier-bed boundary as $\mathbf{v}_m = \big(En_x,\ En_y,\ 0\big) \quad \text{on } \Gamma_b$, where $\mathbf{v}_m$ denotes the boundary mesh velocity, and (n_x, n_y, n_z) represent the components of the outward unit normal vector to the glacier-bed boundary. The erosion rate E is evaluated in (2.3) using the full three-dimensional basal sliding velocity u_b. Consequently, while the erosion rate incorporates the complete three-dimensional flow dynamics, the resulting mesh motion remains restricted to the transverse cross-section, with zero displacement along the longitudinal z-axis.

The numerical model is implemented in COMSOL Multiphysics. The standard finite element formulation is augmented by the GLS stabilization terms described above, while COMSOL is used for finite element assembly, nonlinear solution, and ALE moving-mesh calculations (COMSOL AB, 2022; Donea et al., 1982).

4. Numerical results

Numerical simulations based on the GLS formulation in (3.2) were conducted to investigate three-dimensional glacier flow and long-term glacier-bed evolution in Xue Mountain Glacial Cirque No. 2, Taiwan (Fig. 1). The computational domain, boundary decomposition, and mesh are illustrated in Figure 6. Unless otherwise stated, the reference parameters listed in Table 1 were used throughout the simulations. Specifically, the ice temperature was set to $T = -9°\mathrm{C}$ and the erosion constant to $C_e = 10^{-4}\,\mathrm{a\,m^{-1}}$. A basal sliding constant of $C_b = 40\ \mathrm{m\,a^{-1}\,MPa^{-1}}$ was adopted as the reference value for investigating the effect of ice thickness. This value lies within the range considered in previous numerical simulations of glacial-valley evolution (Seddik et al., 2009). Glacier-bed evolution was simulated over 9 ka, corresponding to the effective duration of glaciation adopted in our previous study (Lee, 2026).

The stabilization parameter α in the GLS formulation (3.2) was tested at values of 0.1, 0.01, and 0.001. Since no significant qualitative differences were observed, $\alpha = 0.1$ was adopted for all subsequent simulations. Equal-order (P_1, P_1) finite elements were used to approximate the velocity and pressure fields.

4.1. Ice thickness sensitivity

The effects of ice thickness H on the glacier-flow field and the resulting glacier-bed evolution are examined below.

Figures 7 and 8 illustrate the spatiotemporal evolution of the velocity and pressure fields, respectively, at $t = 0$ a, 3 ka, 6 ka, and 9 ka. As progressive bed erosion transforms

Algorithm 1 GLS Stokes–erosion solver for the three-dimensional glacier-flow and bed-evolution model.

Initialization: Set the initial glacier-bed geometry, velocity $\mathbf{u}^0$, pressure p^0, and initial time $t_0 = 0$.
Set the evolution time step $\Delta t = 100$ a.
for each time step $i = 0, 1, 2, \ldots$ with $t_i < 9$ ka **do**
    Set the initial nonlinear iterate $\mathbf{u}_0^i = \mathbf{u}^i$, $p_0^i = p^i$, $k = 0$.
    repeat
        Evaluate the regularized Glen viscosity $\eta_k^i = \eta(\mathbf{u}_k^i)$.
        Assemble the linearized Stokes system using η_k^i.
        Solve the GLS finite element system (3.2) for $(\mathbf{u}_{k+1}^i, p_{k+1}^i)$.
        Define $\mathbf{U}_k^i = (\mathbf{u}_k^i, p_k^i)$, and compute relative error as the following Euclidean norm COMSOL AB (2022):

$$\varepsilon_{k+1} = \frac{\|\mathbf{U}_{k+1}^i - \mathbf{U}_k^i\|_{l^2}}{\|\mathbf{U}_k^i\|_{l^2}}.$$

        $k \leftarrow k + 1$.
    until the convergence criterion for ε_k is satisfied.
    Denote the converged flow solution by $\mathbf{u}^{i,*} = \mathbf{u}_k^i$, $p^{i,*} = p_k^i$.
    Determine the magnitude of the three-dimensional basal sliding velocity: $u_b^i = \|\mathbf{u}_t^{i,*}\|$ on Γ_b.
    Compute the basal erosion rate: $E^i = C_e \left(u_b^i\right)^2$.
    Prescribe the erosion-induced mesh velocity projected onto the transverse–vertical (x, y) plane: $\mathbf{v}_m^i = \left(E^i n_x,\ E^i n_y,\ 0\right)$ on Γ_b.
    Update the glacier-bed geometry and computational mesh over the time interval $[t_i, t_{i+1}]$ using the ALE moving-mesh method.
    Set $\mathbf{u}^{i+1} = \mathbf{u}^{i,*}$, $p^{i+1} = p^{i,*}$, as the initial guess for the next time step.
end for

the initial V-shaped profile toward a U-shaped geometry, the maximum flow velocity increases from 9.66 to 10.5 $\mathrm{m\,a^{-1}}$ (Fig. 7). Simultaneously, the subglacial pressure field exhibits strong depth dependence, with peak values concentrated along the valley floor (Fig. 8). Over the 9 ka simulation, the maximum pressure elevates from 1.49×10^5 to 1.65×10^5 Pa. This structural change in pressure distribution directly reflects the progressive widening and deepening of the cross-section during valley morphogenesis.

Figure 9 compares the subglacial pressure distributions at $t = 9$ ka across the considered ice thicknesses ($H = 30$, 40, 50, and 60 m). The maximum pressure increases systematically with H, rising from approximately 1.65×10^5 Pa for $H = 30$ m to 3.09×10^5 Pa for $H = 60$ m, reflecting the enhanced ice overburden. Greater ice thickness amplifies bed-normal lowering, facilitating the progressive cross-sectional transition from an initial V-shaped valley to a classic U-shaped geometry.

Figure 10 illustrates the corresponding glacier-bed profiles and basal-velocity distributions across the valley half-width. As H increases, the resulting bed elevation y_b decreases markedly, with the maximum lowering concentrated along the valley centerline (Fig. 10a). Concurrently, the basal sliding velocity u_b increases systematically with ice thickness, reaching its peak along the valley axis (Fig. 10b).

Overall, the numerical results demonstrate that increasing ice thickness elevates subglacial pressure, accelerates basal sliding velocity, and amplifies bed lowering elevation, with the maximum erosion concentrated along the central axis of the valley.

4.2. Combined effects of ice thickness and basal sliding constant

To further investigate the combined effects of ice thickness H and basal sliding coefficient C_b on long-term valley morphodynamics, additional sensitivity simulations were conducted across the 9 ka evolution period. The predicted bed-normal lowering distances d_b for various combinations of H and C_b are summarized in Table 2.

Table 2: Variation of bed-normal lowering distance d_b with ice thickness H and basal sliding constant C_b.

Ice thicknesses H (m)	Basal sliding constant C_b ($\mathrm{m\,a^{-1}\,MPa^{-1}}$)	Bed-normal lowering distance d_b (m)
30	30	8.04
30	40	15.24
30	50	25.00
40	40	22.55
40	50	38.75
50	40	30.30
60	40	38.57

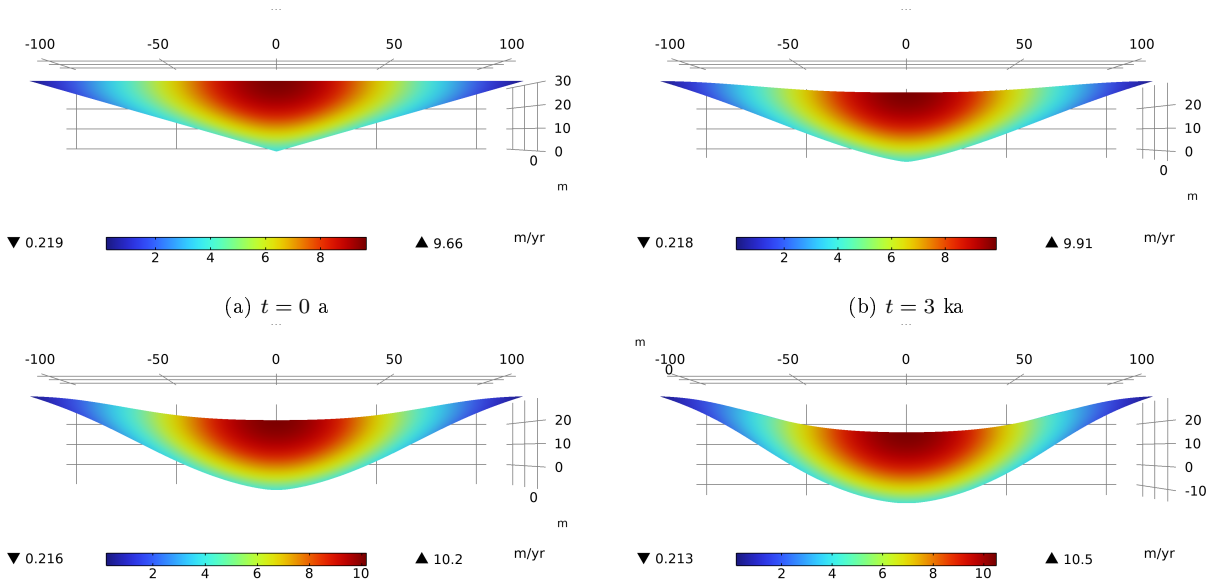

(a) $t = 0$ a (b) $t = 3$ ka

(c) $t = 6$ ka (d) $t = 9$ ka

Figure 7: Spatiotemporal evolution of glacier flow velocity contours for $H = 30$ m at (a) $t = 0$ a, (b) 3 ka, (c) 6 ka, and (d) 9 ka. Maximum flow velocity elevates as progressive erosion transforms the initial V-shaped valley into a U-shaped geometry.

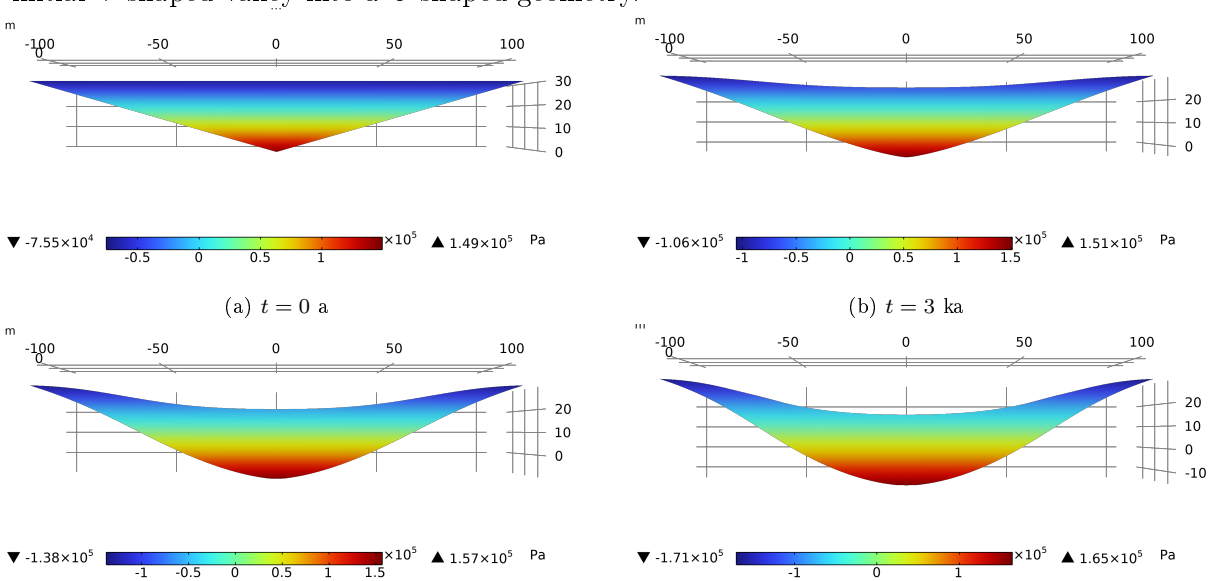

(a) $t = 0$ a (b) $t = 3$ ka

(c) $t = 6$ ka (d) $t = 9$ ka

Figure 8: Spatiotemporal evolution of subglacial pressure contours for $H = 30$ m at (a) $t = 0$ a, (b) 3 ka, (c) 6 ka, and (d) 9 ka. Progressive erosion deepens and widens the valley, driving the transition from a V-shaped to a U-shaped geometry.

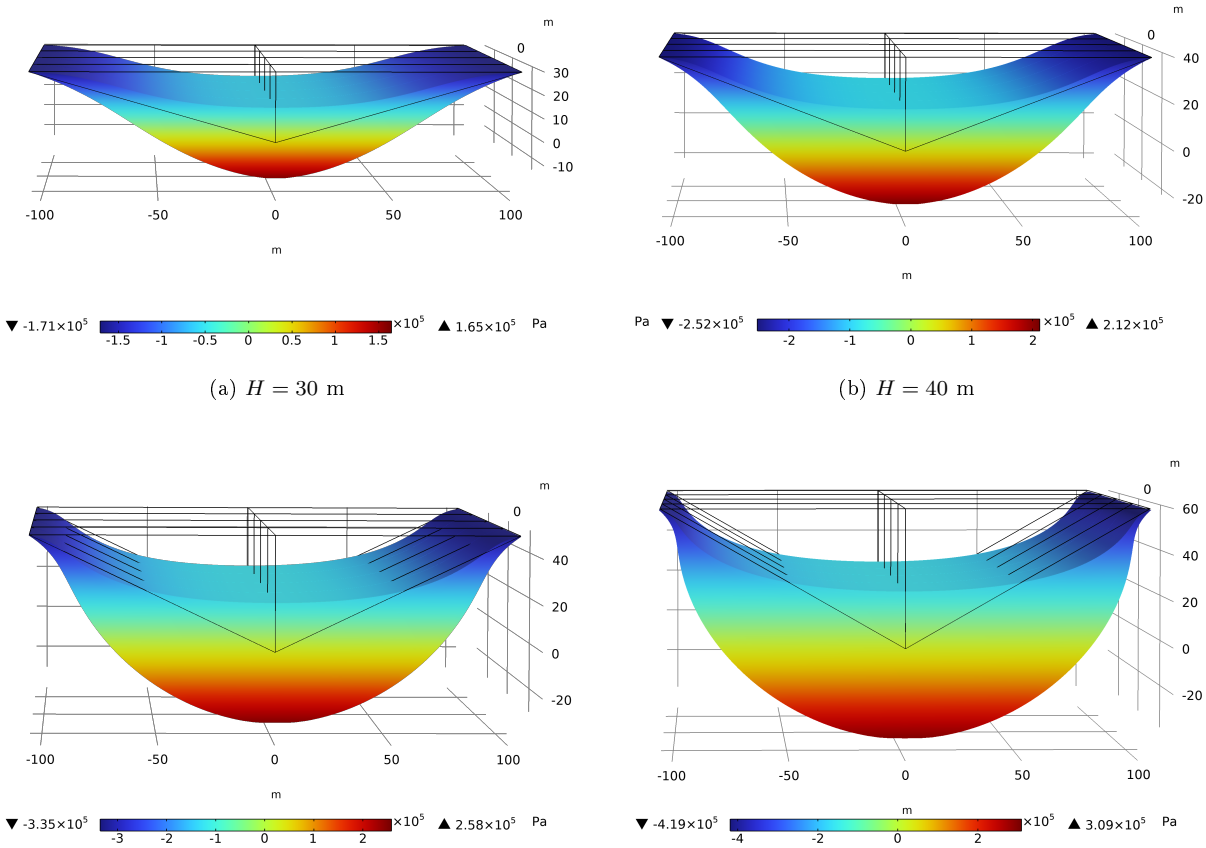

(a) $H = 30$ m

(b) $H = 40$ m

(c) $H = 50$ m

(d) $H = 60$ m

Figure 9: Subglacial pressure distribution at $t = 9$ ka for ice thicknesses of (a) $H = 30$ m, (b) $H = 40$ m, (c) $H = 50$ m, and (d) $H = 60$ m. Increasing ice thickness elevates subglacial pressure and enhances bed-normal lowering, driving the transition from a V-shaped to a U-shaped valley.

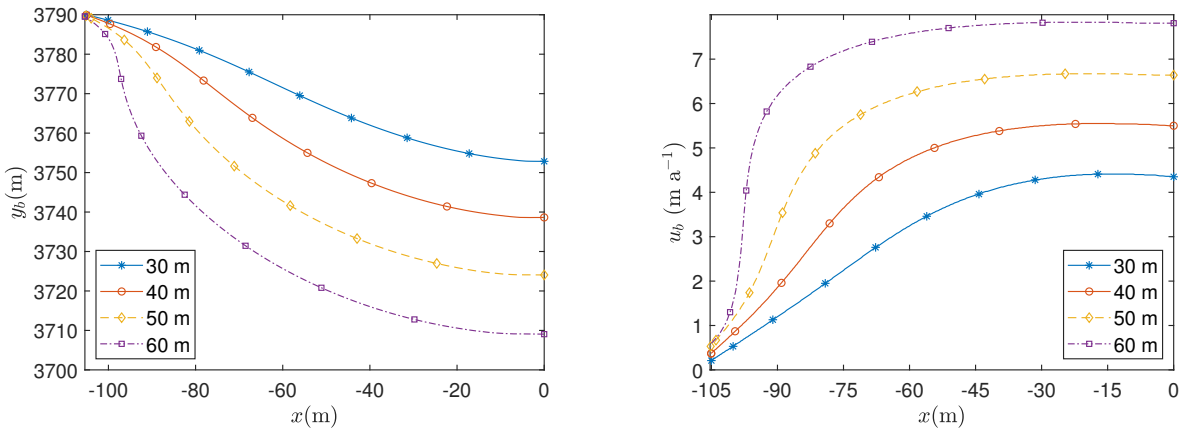

(a) Evolution of the glacier-bed elevation

(b) Evolution of the basal velocity

Figure 10: Glacier-bed and basal-velocity profiles across the cross-valley half-width at $t = 9$ ka for ice thicknesses of $H = 30$–60 m. (a) Bed elevation y_b decreases with increasing H, with maximum erosion concentrated along the valley axis. (b) Basal sliding velocity u_b increases systematically with H, reaching its peak near the centerline.

At a fixed ice thickness of $H = 30$ m, d_b increases markedly from 8.04 to 25.00 m as C_b increases from 30 to 50 m a^{-1} MPa^{-1}. Similarly, for a constant $C_b = 40$ m a^{-1} MPa^{-1}, d_b increases from 15.24 to 38.57 m as H increases from 30 to 60 m. These results demonstrate that both H and C_b exert primary controls on the cumulative bed-normal lowering distance.

Furthermore, the influence of C_b on d_b amplifies with increasing ice thickness. For instance, raising C_b from 40 to 50 m a^{-1} MPa^{-1} expands d_b by 9.76 m (from 15.24 to 25.00 m) at $H = 30$ m, whereas the identical increment in C_b leads to a 16.20 m expansion in d_b (from 22.55 to 38.75 m) at $H = 40$ m. This difference indicates an interaction between ice thickness and the basal sliding constant, whereby thicker ice amplifies the effect of basal sliding on bed erosion.

To quantify this dynamic coupling, the simulated d_b values were fitted using a two-variable polynomial regression model incorporating an interaction term: $d_b = w_1 H + w_2 C_b + w_3 H C_b + d_0$. The resulting empirical response surface is expressed as

$$d_b = -2.054H - 1.247C_b + 0.070HC_b + 43.599, \tag{4.1}$$

yielding a coefficient of determination $R^2 = 0.997$ and a root-mean-square error (RMSE) of 0.554 m.

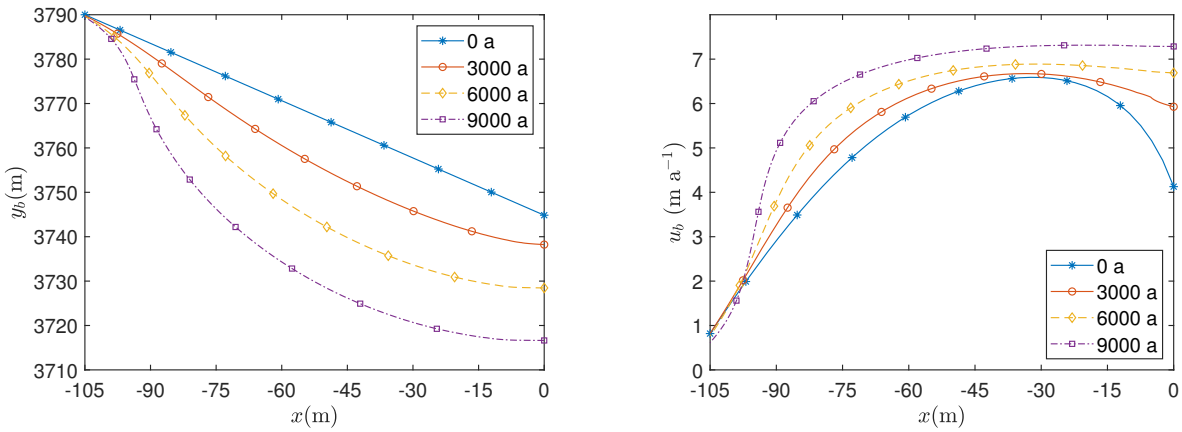

(a) Evolution of glacier-bed elevation

(b) Evolution of basal velocity

Figure 11: Evolution of glacier-bed elevation and basal-velocity profiles over half of the glacier valley from $t = 0$ to 9 ka for $H = 55$ m. (a) Bed lowering is greatest near the valley center. (b) Basal velocity increases while maintaining a similar transverse distribution.

4.3. Comparison with the Present-Day Valley Cross-Profile

For $C_b = 40$ m a^{-1} MPa^{-1}, substituting the fitted relationship for d_b in (4.1) into the topographic constraint in (2.2) yields an estimated ice thickness of $H \approx 55.4$ m. Accordingly, an ice thickness of $H = 55$ m was adopted for the baseline three-dimensional simulation to evaluate glacier-bed evolution and compare the simulated cross-profile with present-day observations.

Figure 11 further illustrates the temporal evolution of the glacier-bed and basal-velocity profiles for $H = 55$ m. As the simulation proceeds, the glacier bed is progressively lowered, with the most pronounced change occurring near the valley center, where the bed elevation decreases from approximately 3744.8 m to 3716.6 m over 9 ka (Fig. 11a). The basal-velocity profile retains a self-similar overall shape throughout the simulation, while the magnitude of basal sliding increases systematically over time. At the valley center ($x = 0$ m), the basal velocity increases from approximately 4.1 to 7.2 m a^{-1} (Fig. 11b). Furthermore, the maximum basal velocity elevates and progressively shifts toward the valley center as the glacier bed evolves.

The valley geometries simulated after 9 ka are compared with the present-day cross-profile in Figure 12. For the baseline scenario ($H = 55$ m and $C_b = 40$ m a^{-1} MPa^{-1}), the simulated bed profile lies slightly below the present-day profile across most of the transverse section while maintaining a smooth, characteristic U-shaped morphology. The simulated minimum bed elevation reaches 3716.6 m, departing by merely 0.6 m from

the present-day observed value of 3716.0 m. This exceptional agreement indicates that $H = 55$ m provides a physically plausible reconstruction of the paleo-glacier state under modern topographic constraints.

To further assess the predictive capability of (4.1), the fitted relationship was combined with the geometric constraint in (2.2), with $C_b = 50\ \mathrm{m\,a^{-1}\,MPa^{-1}}$, yielding an estimated ice thickness of $H \approx 45$ m. This parameter combination was not included in the regression dataset listed in Table 2 and was subsequently evaluated through an independent numerical simulation. The simulation yields a minimum bed elevation of 3714.8 m, only 1.2 m below the present-day value of 3716.0 m.

Finally, Figure 13 summarizes the simulated and reconstructed cases within the H–C_b parameter space based on the fitted bed-normal lowering relationship in (4.1). The baseline scenario ($H = 55$ m, $C_b = 40\ \mathrm{m\,a^{-1}\,MPa^{-1}}$) and the independent validation case ($H = 45$ m, $C_b = 50\ \mathrm{m\,a^{-1}\,MPa^{-1}}$) are highlighted alongside the simulations in Table2 used to construct the regression model. The curved contours in Figure 13 further illustrate the non-linear coupling between H and C_b, demonstrating that increasing ice thickness amplifies the sensitivity of d_b to variations in C_b across the explored parameter space.

5. Discussion

The three-dimensional numerical simulations presented here provide a mechanistic framework for evaluating how ice deformation, basal sliding, and bedrock erosion jointly transform an initially V-shaped alpine valley into a characteristic U-shaped glacial cirque over millennial time scales. Basal erosion is strongly concentrated along the valley axis, driving progressive deepening and lateral widening of the cross-section. Meanwhile, the transverse basal-velocity profile maintains a self-similar distribution throughout the evolution, even as its overall magnitude increases with time. This behavior suggests that the development of the U-shaped valley is driven primarily by the spatial concentration and progressive intensification of basal erosion, rather than by a fundamental spatial reorganization of the glacier-flow field.

Sensitivity experiments further demonstrate the coupled control of ice thickness H and basal sliding constant C_b on cumulative bed-normal lowering. Increasing either parameter enhances d_b, while the non-linear coupling interaction term in (4.1) indicates that the influence of C_b amplifies with ice thickness across the explored parameter space. This dynamic behavior is physically consistent with the adopted erosion formulation ($E = C_e u_b^2$), as both H and C_b directly govern the basal velocity field u_b, which exerts a non-linear effect on erosion rate. Furthermore, an additional numerical simulation ($H \approx 45$ m, $C_b = 50\ \mathrm{m\,a^{-1}\,MPa^{-1}}$), using a parameter combination inferred from the

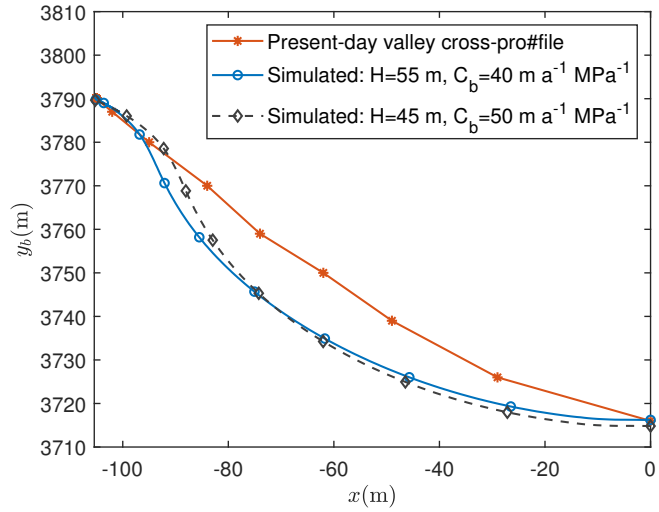

Figure 12: Comparison of the present-day valley half-profile with the simulated baseline ($H = 55$ m, $C_b = 40\ \mathrm{m\,a^{-1}\,MPa^{-1}}$) and additional ($H = 45$ m, $C_b = 50\ \mathrm{m\,a^{-1}\,MPa^{-1}}$) scenarios after 9 ka.

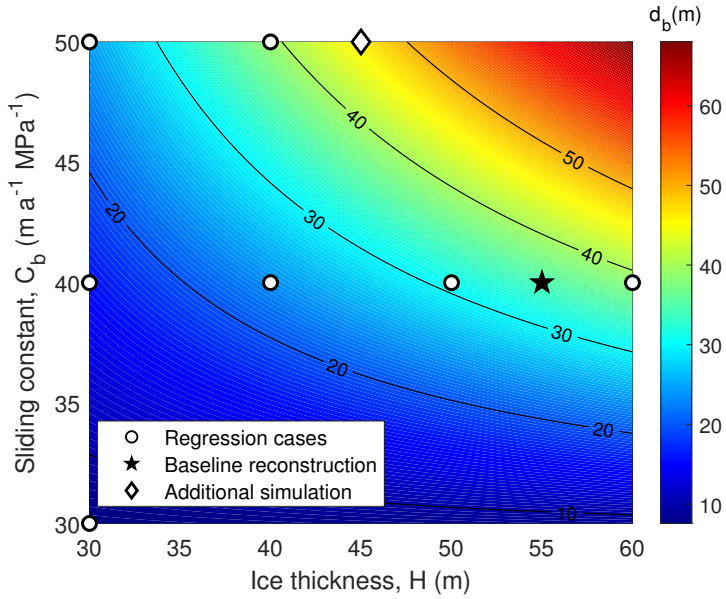

Figure 13: Response surface of the fitted bed-normal lowering distance $d_b(H, C_b)$ after 9 ka of evolution. Circles denote numerical simulations used in the regression fit, while the star and diamond represent the baseline scenario and independent validation test, respectively.

fitted relationship and the geomorphic constraint, yields a minimum bed elevation of 3714.8 m, only 1.2 m below the present-day value. This result supports the predictive use of the empirical response surface within the explored parameter space. Nevertheless, the reconstructed ice thickness ($H \approx 55$ m) should be interpreted as a physically plausible scenario constrained by the prescribed sliding and erosion parameters over the assumed 9 ka evolution period, rather than a unique deterministic solution for former glacier dimensions.

Several simplifications and numerical considerations inherent to the current computational framework warrant evaluation. Complex subglacial process-mechanisms are parameterized via an empirical erosion relationship ($E = C_e u_b^2$) with spatially uniform coefficients, while erosion-induced mesh displacement is constrained to the transverse-vertical plane. From a computational perspective, the application of the stabilized equal-order GLS formulation is critical for ensuring numerical robustness; it effectively suppresses spurious pressure oscillations inherent to equal-order (P_1-P_1) element pairs without imposing the stringent inf-sup conditions required by mixed finite-element schemes. This stabilization helps maintain stable pressure and velocity fields across 90 successive mesh updates over the 9 ka simulation period.

However, physical subglacial processes such as spatially variable basal traction, subglacial quarrying and plucking, transient subglacial hydrology, sediment transport, and time-dependent climatic forcing are not explicitly resolved. Additionally, the empirical response surface relating d_b, H, and C_b is parameterized over a specific domain and should be extrapolated beyond the explored parameter bounds with caution. Consequently, the simulation results represent a physically grounded evolutionary pathway rather than a deterministic history of Xue Mountain Glacial Cirque No. 2.

Despite these necessary simplifications, the close agreement between the simulated bed profile and the present-day valley geometry demonstrates that the integrated flow-sliding-erosion model successfully captures the primary morphological evolution of the cirque over a 9 ka time scale. More broadly, these results illustrate how past alpine glaciation has imprinted a persistent geomorphic legacy in subtropical mountain environments. Such inherited glacial topography provides a crucial physical template for understanding the spatial organization and habitat isolation of high-elevation ecosystems. Comparative phylogeographic studies of alpine biota in Taiwan such as endemic mountain-dwelling ground beetles indicate that Quaternary climate-driven landscape modifications significantly facilitated population divergence and genetic structuring (Weng et al., 2016). Although such biogeographical consequences lie beyond the scope of the present physical model, the reconstructed glacial landscape provides a compelling quantitative foundation for future interdisciplinary investigations bridging alpine geomorphology, phylogeography, and biodiversity conservation in subtropical island arcs.

6. Conclusions

In this study, a three-dimensional ice-flow model coupled with basal sliding and bedrock erosion under an Arbitrary Lagrangian-Eulerian (ALE) moving-mesh framework was developed to investigate the millennial-scale valley morphodynamics of Xue Mountain Glacial Cirque No. 2, Taiwan. The main findings are summarized as follows:

1. The stabilized equal-order GLS finite-element formulation helps suppress spurious pressure oscillations without requiring stringent inf-sup conditions. It provides a highly robust and computationally efficient framework for resolving coupled 3D ice dynamics and moving-boundary evolution across 90 geometry updates over a 9 ka time scale.
2. Simulation results demonstrate that basal erosion is strongly concentrated along the valley axis, driving the progressive morphological transition from an initial V-shaped valley into a characteristic U-shaped glacial valley.
3. Under a fixed basal sliding constant, the simulated bed-normal lowering distance d_b exhibits an approximately linear relationship with ice thickness H across the explored parameter domain.
4. Sensitivity analyses demonstrate that the basal sliding constant C_b and ice thickness H exert strong, coupled controls on d_b. Increasing either parameter enhances bed lowering, while the non-linear coupling interaction term in (4.1) indicates that higher ice thicknesses amplify the sensitivity of d_b to variations in C_b within the explored parameter space.
5. Using the present-day valley-floor elevation as a geomorphic constraint, the baseline scenario ($H = 55$ m, $C_b = 40\ \mathrm{m\,a^{-1}\,MPa^{-1}}$) yields a minimum bed elevation of 3716.6 m, only 0.6 m above the observed value. An independent simulation ($H = 45$ m, $C_b = 50\ \mathrm{m\,a^{-1}\,MPa^{-1}}$), with ice thickness inferred from the fitted relationship, yields 3714.8 m, only 1.2 m below the observed value, supporting the predictive capability of the empirical response surface.

Overall, this work demonstrates the application of the stabilized equal-order GLS formulation to fully three-dimensional, coupled ice-flow and bed-evolution modeling. When applied to a subtropical alpine landscape, the quantitative framework successfully links ice-flow dynamics, subglacial erosion, and millennial-scale morphodynamics, highlighting the persistent geomorphic legacy left by past alpine glaciation.

Data availability

The present-day and idealized valley-geometry data and MATLAB script supporting this study are available in Zenodo at https://doi.org/10.5281/zenodo.22885913.

Acknowledgements

The author gratefully acknowledges the financial support provided in part by the National Science and Technology Council(Taiwan) [114-2115-M-160-001-MY2].

Declaration of generative AI and AI-assisted technologies in the manuscript preparation process

During the preparation of this manuscript, the author used ChatGPT (OpenAI) and Gemini (Google) to assist with English-language editing and grammar checking. The author reviewed and edited the content as needed and takes full responsibility for the content of the published article.

References

R. Asami et al., *Last glacial temperature reconstructions using coupled isotopic analyses of fossil snails and stalagmites from archaeological caves in Okinawa, Japan*, Scientific Reports 11 (2021), 21922. doi: 10.1038/s41598-021-01484-z.

S. C. Brenner and L. R. Scott, *The Mathematical Theory of Finite Element Methods*, 3rd ed., Springer, New York, 2008. doi: 10.1007/978-0-387-75934-0.

Q. Chen, M. Gunzburger and M. Perego, *Well-posedness results for a nonlinear Stokes problem arising in glaciology*, SIAM J. Math. Anal. 45 (2013), 2710–2733. doi: 10.1137/110848694.

P. U. Clark, A. S. Dyke, J. D. Shakun, A. E. Carlson, J. Clark, B. Wohlfarth, J. X. Mitrovica, S. W. Hostetler and A. M. McCabe, *The Last Glacial Maximum*, Science 325 (2009), 710–714. doi: 10.1126/science.1172873.

COMSOL AB, *COMSOL Multiphysics® v6.1*, COMSOL AB, Stockholm, Sweden, 2022.

Z. Cui, C. Yang, G. Liu, W. Zhang, S. Wang and Q. Sung, *The Quaternary glaciation of Shesan Mountain in Taiwan and glacial classification in monsoon areas*, Quatern. Int. 97–98 (2002), 147–153. doi: 10.1016/S1040-6182(02)00060-5.

J. Donea, S. Giuliani and J.-P. Halleux, *An arbitrary Lagrangian–Eulerian finite element method for transient dynamic fluid-structure interactions*, Comput. Methods Appl. Mech. Engrg. 33 (1982), 689–723. doi: 10.1016/0045-7825(82)90128-1.

J. Donea and A. Huerta, *Finite Element Methods for Flow Problems*, John Wiley & Sons, Chichester, 2003. doi: 10.1002/0470013826.

D. L. Egholm, V. K. Pedersen, M. F. Knudsen and N. K. Larsen, *Coupling the flow of ice, water, and sediment in a glacial landscape evolution model*, Geomorphology 141–142 (2012), 47–66. doi: 10.1016/j.geomorph.2011.12.019.

D. L. Egholm, V. K. Pedersen, M. F. Knudsen and N. K. Larsen, *On the importance of higher order ice dynamics for glacial landscape evolution*, Geomorphology 141–142 (2012), 67–80. doi: 10.1016/j.geomorph.2011.12.020.

V. Girault and P.-A. Raviart, *Finite Element Methods for Navier–Stokes Equations: Theory and Algorithms*, Springer, Berlin, 1986. doi: 10.1007/978-3-642-61623-5.

J. W. Glen, *The creep of polycrystalline ice*, Proc. R. Soc. Lond. A 228 (1955), 519–538. doi: 10.1098/rspa.1955.0066.

Google, *Google Earth Pro*, online resource, accessed September 12, 2021.

R. Greve, *On non-dimensional forms of basal sliding laws and flow laws for ice-sheet and glacier modelling*, J. Glaciol. 71 (2025), e123, 1–6. doi: 10.1017/jog.2025.10100.

R. Greve and H. Blatter, *Dynamics of Ice Sheets and Glaciers*, Springer, Berlin, 2009. doi: 10.1007/978-3-642-03415-2.

B. Hallet, *A theoretical model of glacial abrasion*, J. Glaciol. 23 (1979), 39–50. doi: 10.3189/S0022143000029725.

Happyman GIS Project, *Taiwan Online Topographic Map*, online resource, accessed February 17, 2025.

J. M. Harbor, *Numerical modeling of the development of U-shaped valleys by glacial erosion*, Geol. Soc. Am. Bull. 104 (1992), 1364–1375. doi: 10.1130/0016-7606(1992)104<1364:NMOTDO>2.3.CO;2.

S. S. R. Jamieson, N. R. J. Hulton and M. Hagdorn, *Modelling landscape evolution under ice sheets*, Geomorphology 97 (2008), 91–108. doi: 10.1016/j.geomorph.2007.02.047.

T. Kano, *Shan, Yun Yu Fanren: Taiwan Gaoshan Jixing [Mountains, Clouds, and Indigenous Peoples: Travels in Taiwan's High Mountains]*, translated by N.-C. Yang, Yushan Publishing, Taipei, 2000.

H.-C. Lee, *Finite element modelling of glacier-bed evolution: A case study of Xue Mountain Cirque No. 2, Taiwan*, J. Chin. Inst. Eng. (2026), Advance Publication, 1–13. doi: 10.1080/02533839.2026.2669183.

H.-C. Lee, M.-H. Chen, J. Chu and M.-C. Shiue, *Numerical simulation of basal crevasses of the tidewater glacier with Galerkin least-squares finite element method*, J. Eng. Math. 145 (2024), 17. doi: 10.1007/s10665-024-10356-0.

H.-C. Lee and H. Lee, *Stabilized equal lower-order finite element methods for simulating Brinkman equations in porous media*, Int. J. Comput. Math. 101 (2024), 1132–1151. doi: 10.1080/00207160.2024.2343102.

H.-C. Lee and H. Lee, *A Galerkin least-squares finite element method within deep neural networks for efficient simulation of generalized Newtonian flows in porous media*, J. Comput. Appl. Math. 482 (2026), 117331. doi: 10.1016/j.cam.2025.117331.

H.-C. Lee and H. Lee, *A stabilized equal-order finite element method for nonlinear Stokes problems with applications to glacier flow*, Taiwanese J. Math. (2026), Advance Publication, 1–28. doi: 10.11650/tjm/260506.

K. R. MacGregor, R. S. Anderson, S. P. Anderson and E. D. Waddington, *Numerical simulations of glacial-valley longitudinal profile evolution*, Geology 28 (2000), 1031–1034. doi: 10.1130/0091-7613(2000)28<1031:NSOGLP>2.0.CO;2.

I. Monnesland, E. Lee, M. Gunzburger and R. Yoon, *A least-squares finite element method for a nonlinear Stokes problem in glaciology*, Comput. Math. Appl. 71 (2016), 2421–2431. doi: 10.1016/j.camwa.2015.11.001.

National Parks of Taiwan, *National Parks of Taiwan*, online resource, accessed August 24, 2026.

C.-L. Navier, *Mémoire sur les lois du mouvement des fluides*, Mém. Acad. R. Sci. Inst. France 6 (1823), 389–440.

H. Seddik, R. Greve, S. Sugiyama and R. Naruse, *Numerical simulation of the evolution of glacial valley cross sections*, arXiv:0901.1177 [physics.geo-ph] (2009).

SpaceClaim Corporation, *Creating a Spline*, online documentation, accessed March 30, 2026.

Y.-M. Weng, M.-M. Yang and W.-B. Yeh, *A comparative phylogeographic study reveals discordant evolutionary histories of alpine ground beetles (Coleoptera, Carabidae)*, Ecology and Evolution 6 (2016), 2061–2073. doi: 10.1002/ece3.2006.

S. H. Yang and Y. L. Shi, *Three-dimensional numerical simulation of glacial trough forming process*, Sci. China Earth Sci. 58 (2015), 1656–1668. doi: 10.1007/s11430-015-5120-8.